

See discussions, stats, and author profiles for this publication at: <https://www.researchgate.net/publication/49767821>

# Quantitative annular dark-field STEM images of a silicon crystal using a large-angle convergent electron probe with a 300-kV cold field-emission gun

Article in Journal of electron microscopy · April 2011

DOI: 10.1093/jmicro/dfq084 · Source: PubMed

CITATIONS

29

READS

158

9 authors, including:



Suhyun Kim  
Samsung

17 PUBLICATIONS 149 CITATIONS

[SEE PROFILE](#)



Yoshifumi Oshima  
Japan Advanced Institute of Science and Technology

137 PUBLICATIONS 1,352 CITATIONS

[SEE PROFILE](#)



Yukihito Kondo  
JEOL

177 PUBLICATIONS 4,773 CITATIONS

[SEE PROFILE](#)



Masaki Takeguchi  
National Institute for Materials Science

140 PUBLICATIONS 1,281 CITATIONS

[SEE PROFILE](#)

Some of the authors of this publication are also working on these related projects:



Fabrication of hydrazine sensor based on silica-coated Fe<sub>2</sub>O<sub>3</sub> magnetic nanoparticles prepared by a rapid microwave irradiation method [View project](#)



Atomic resolved STEM observation of Thermoelectric materials [View project](#)



Physical: Full-length

# Quantitative annular dark-field STEM images of a silicon crystal using a large-angle convergent electron probe with a 300-kV cold field-emission gun

Suhyun Kim<sup>1,\*</sup>, Yoshifumi Oshima<sup>2</sup>, Hidetaka Sawada<sup>3</sup>,  
Toshikatsu Kaneyama<sup>3</sup>, Yukihiro Kondo<sup>3</sup>, Masaki Takeguchi<sup>4</sup>,  
Yoshiko Nakayama<sup>4</sup>, Yasumasa Tanishiro<sup>1</sup> and Kunio Takayanagi<sup>1</sup>

<sup>1</sup>Department of Physics, Tokyo Institute of Technology, 2-12-1, 1-24 Oh-okayama, Meguro-ku, Tokyo 152-8551, Japan, <sup>2</sup>Research Center for Ultra HVEM, Osaka University, 7-1 Mihogaoka, Osaka, Ibaraki 567-0047, Japan, <sup>3</sup>Japan Electron Optics Laboratory (JEOL), 3-1-2 Musashino, Akishima, Tokyo 196-8558, Japan and <sup>4</sup>National Institute for Material Science (NIMS), 3-13, Sakura, Tsukuba, Ibaraki 305-0047, Japan

\*To whom correspondence should be addressed. E-mail: suhyun.k.aa@m.titech.ac.jp

**Abstract** Annular dark-field scanning transmission electron microscope (ADF-STEM) images of an Si (001) crystal were obtained by using an aberration-corrected electron microscope, at 30-mrad convergent probe and cold field-emission gun at 300 kV. The intensity of ADF-STEM images, that is, the number of scattered electrons relative to the incident electrons, obtained for specimen thickness from 10 to 50 nm was compared quantitatively with absorptive multi-slice simulation. The column and background intensities were analyzed by column-by-column two-dimensional Gaussian fitting. These intensities were found to increase linearly with the sample thicknesses. However, the simulated image gave higher column intensity and lower background intensity for all the sample thickness. We found that experimental images were reproduced by the simulation with Gaussian convolution of 70 pm full-width at half-maximum for all the sample thicknesses from 10 to 50 nm. The possible factors accounted for this Gaussian convolution is discussed.

**Keywords** STEM, HAADF, Z-contrast, silicon, aberration correction, quantitative analysis

**Received** 27 October 2010, accepted 24 December 2010

## Introduction

Three-dimensional structure (elementary) analysis of nano-scale materials is increasingly important for gaining an understanding of the properties of electronic devices [1–3], catalysis [4], rechargeable batteries [5], and so on. A homogeneous dilute dopant density in the channel region [6,7] is necessary to control the gate threshold voltage of silicon-based nano-devices. In homogeneity and/or localization results in clustering of dopants that suppress the carrier concentration [8–10]. High-angle annular

dark-field scanning transmission electron microscopy (HAADF-STEM) has been successfully used to detect heavy dopant atoms such as antimony (Sb) in silicon crystals [11].

Recently, spherical aberration (Cs)-corrected electron microscopes (SAC-EMs) have improved the spatial resolution of HAADF imaging [12]. SAC-EMs have also improved the depth resolution, as demonstrated with hafnium atoms in an amorphous layer of SiO<sub>2</sub> [13]. The increased depth resolution afforded by the use of a large convergent

angle of 30 mrad (300 kV) has enabled light arsenic (As) dopants to be detected in silicon crystals [14]. Improved depth resolution by large convergent angles had enabled clusters to be detected, as reported previously [15].

The previous STEM experiments compared the column intensities of the experimental HAADF images with those of the simulated ones by the global scaling [16,17]. Recently, LeBeau and Stemmer counted the number of electrons falling onto an annular detector [18] and compared the absolute intensities of experimental and simulated HAADF images of crystals containing heavy elements such as  $\text{SrTiO}_3$  and  $\text{PbWO}_4$  [19–21]. Although the absolute intensity of the experimental images did not match that of the simulated images, they found that it matched that of the simulated image after convolving it by a Gaussian function. They suggested that the discrepancy between the experimental and simulated images came from spatial incoherence stemming from the effective size of the source, mechanical instability of the microscope, drift, and so on [19–21]. To detect homogeneities and clustering of dopants quantitatively, it is important to find a factor that covers the mismatch between the absolute intensities of the experiment and simulation for a large convergent angle of incident probe.

In this study, we performed a quantitative analysis of ADF images of non-doped silicon crystals with thicknesses from 10 to 50 nm. A multi-slice simulation based on the absorptive potential approximation was used for quantitative comparison with the experiment [22]. We found that the simulated ADF images convolved with a Gaussian function of 70 pm full-width at half-maximum (FWHM) reproduced the experimental ones for all the sample thicknesses. We discuss possible factors accounted for 70 pm Gaussian convolution.

## Methods

An aberration-corrected electron microscope (R005) fitted with a cold field-emission gun (CFEG) was used at an accelerating voltage of 300 kV [23]. Chromatic aberration,  $C_c$ , was 1.65 mm and energy spread was 0.5 eV. The incident convergent angle was 30 mrad. This corresponds to  $0.76 \text{ \AA}^{-1}$  of the

scattering vector,  $\sin \theta_B/\lambda$ , where  $\theta_B$  is the Bragg angle and  $\lambda = 0.019 \text{ \AA}$  is the wavelength of the electron at 300 kV. The ADF detector had inner–outer angles of 42–104 mrad ( $1.06\text{--}2.64 \text{ \AA}^{-1}$ ). The inner angle was relatively lower than that used in the previous experiments [24]. The silicon crystal was viewed from the [001]-direction. The thickness was measured by electron energy loss spectroscopy (EELS).

The ADF images were recorded at the focus that gave the highest column intensity by adjusting the amount of defocus in steps of 1 nm. The spherical aberration was corrected by using the SRAM method [25]. The ADF images had a frame size of  $512 \times 512$  pixels. The size of each pixel was 9.1 pm. The dwell time,  $t$ , per pixel (the time that probe spends at each pixel) was 38  $\mu\text{s}$ . The probe current,  $I_{\text{Probe}}$ , was measured to be constant (30 pA) before and after acquisition of the ADF image. Therefore, the number of incident electrons for each pixel was about 7000, as calculated from  $t \cdot I_{\text{Probe}}/e$ , where  $e$  is the elementary charge. For quantitative imaging, the intensity of the ADF detector output for the incident electron was calibrated, following the method described by LeBeau and Stemmer [18]. Figure 1 shows the calibration curve: the ADF image intensity was proportional to the number of electrons falling on the detector in the range 0–250 electrons. Since the ADF image intensities of an Si crystal acquired in the experiment were smaller than 250, the intensity was converted into the number of electrons by using the linear relationship given in Fig. 1.

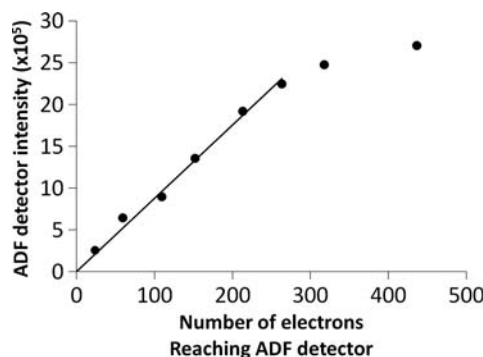


**Fig. 1.** Relationship between the number of electrons falling onto the annular detector and intensity of the STEM image. The experimental data are plotted (dots). The ADF intensity was proportional to the number of electrons up to 250 electrons.

The Si (001) sample was prepared by mechanical polishing to be electron-transparent. Compared with the sample prepared by ion milling (not shown here), the mechanically polished specimen showed ADF images with less fluctuation in the column intensities and less blurring of the column image. The surface of the ion-milled specimen can have a damaged layer which causes a blurred image intensity [26].

The thickness of the specimen was estimated by EELS to be from 10 to 50 nm. The EELS spectrum was obtained with an aperture size of 2.1 mrad by averaging 50 measurements, each of which was obtained with exposure time of 0.05 s and energy dispersion of 0.1 eV/channel. The specimen thickness was calculated by multiplying the inelastic mean free path  $\lambda_B$  (230 nm for Si) with the logarithm of the ratio of the total area to zero-loss area [27].

The ADF intensity of each column (column intensity) was obtained by 2D Gaussian function fitting to the raw data [14]:

$$I = I_P \exp\left(-\frac{(x-x_0)^2}{2\sigma^2}\right) \exp\left(-\frac{(y-y_0)^2}{2\sigma^2}\right) + I_B. \quad (1)$$

Here,  $(x_0, y_0)$  is the coordinate of the column and  $\sigma$  is the standard deviation. The FWHM of the column image is given by  $2.35\sigma$ . The fitting was performed using the Levenberg–Marquardt algorithm, which is a standard nonlinear fitting method [28]. The column intensity,  $I_C = I_P + I_B$ , was defined as the sum of the Gaussian amplitude,  $I_P$ , and the background,  $I_B$ . The ADF image intensity for each pixel was normalized by the number of incident electrons.

## Simulation

The multi-slice simulation was performed by running the HREM<sup>TM</sup> program [22], including (thermal diffuse scattering (TDS)) absorptive potential approximation that used the Weikenmeier–Kohl scattering factor. A Debye–Waller factor (DWF) of  $0.46 \text{ \AA}^2$  was used for Si atoms [29]. The cut-off scattering vector,  $\sin \theta_B/\lambda$ , was determined to be  $3 \text{ \AA}^{-1}$ , which corresponded to a scattering angle of 120 mrad. Regarding the reciprocal-space resolution for obtaining the transmitted and diffracted disk

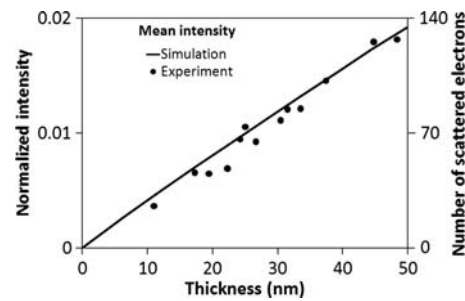
patterns, the Fourier coefficients were calculated at  $512 \times 512$  points in the square of  $\pm 3 \text{ \AA}^{-1}$ . The intensity was calculated at  $101 \times 101$  points per silicon unit cell ( $0.543 \text{ nm}^2$ ). The silicon unit cell of the calculation was divided into four slices, and the simulated image or intensity profile was calculated up to 50 nm in thickness (368 slices). The defocus was chosen to be 2 nm below the top specimen surface (underfocus), where the column intensity had the maximum [15].

The ADF intensity for a chromatic beam of  $\Delta E = 0.5 \text{ eV}$  was calculated by summing a monochromatic ADF intensities within a defocus spread of  $\Delta f = 0.5Cc(\Delta E/E)$ . The column intensity  $I_C$  did not change by more than 3%. Therefore, we compared the monochromatic images with the experimental images hereafter.

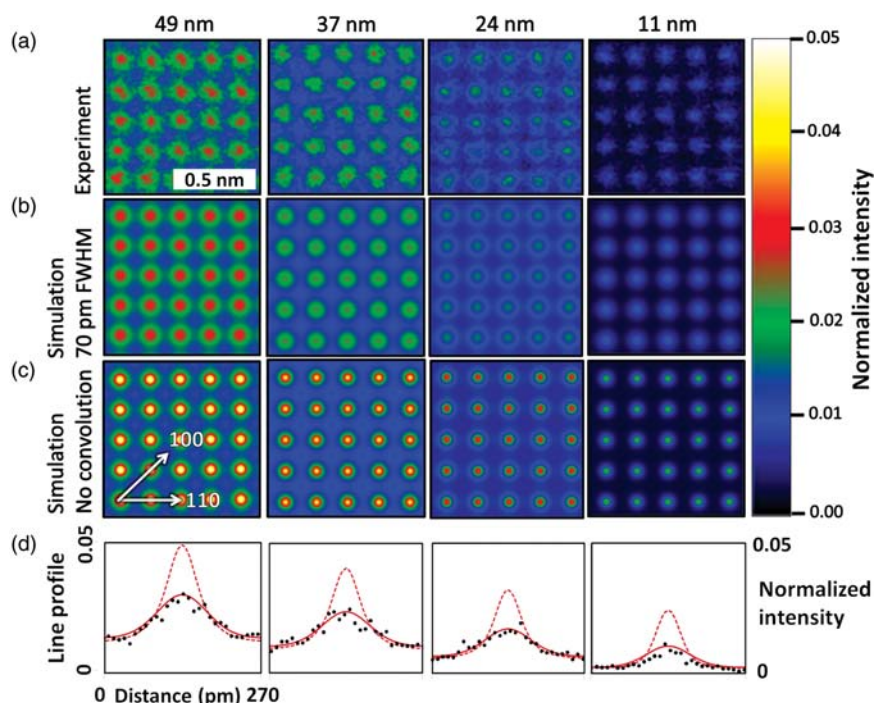
## Result

Figure 2 shows mean intensity,  $I_M$ , as a function of thickness. It is defined by the intensity of scattered electrons per unit area of the ADF-STEM image and was calculated by summing the intensities of all pixels in an unit area of the STEM image [20]. In Fig. 2, simulated mean intensity (solid line) had the same value as the experimental intensity (circles).

The first row of Fig. 3 shows the ADF images observed at thicknesses of 49, 37, 24 and 11 m. The intensities are displayed as a rainbow of colors. The images in the third row are the simulations. The simulated column intensity does not match the observed one; the simulated column has a much sharper profile than the experimental one. After convolving the simulated image by a Gaussian



**Fig. 2.** Mean intensity of all pixels in the ADF image as a function of thickness (nm). Fourteen experimental mean intensities, for which the thicknesses are different, are plotted (dots). The simulated mean intensity is drawn as a function of thickness. The experimental intensities are almost on the simulated line.



**Fig. 3.** (a) Typical ADF images taken at thicknesses of 49, 37, 24 and 11 nm. No drift correction was done because the images show little drift. Intensity ratio of the number of electrons falling onto the annular detector to that of incident electrons is shown in rainbow colors on the bar on the right side. (b) Simulated ADF images with a Gaussian convolution of 70 pm (FWHM) for thicknesses of 49, 37, 24 and 11 nm. The simulated images match the observed images. (c) Simulated ADF images without Gaussian convolution. (d) Typical intensity profiles of one Si column in [100]-direction. dot: experiment, solid line: simulation with Gaussian convolution, dashed line: simulation without convolution.

envelope function with an FWHM of 70 pm, the theoretical results were able to reproduce all of the experimental images from different specimen thicknesses as shown in the second row of Fig. 3. The intensity profiles of the images in the first, second, and third rows are shown in the fourth row; the experimental profiles were reproduced by a Gaussian with an FWHM of 70 pm.

The same Gaussian convolution provided a good agreement with the 14 experimental images of thicknesses ranging from 10 to 50 nm, as displayed in Fig. 4.

Figure 4(a) and (b) shows the coincidence between the experimental intensities and the simulated ones with the 70 pm FWHM Gaussian convolution. The column intensities, background intensity, and FWHMs of Si columns for the thickness range 10–50 nm coincide for a 70 pm Gaussian convolution. As shown in Fig. 4(a), the simulated column intensity without the Gaussian convolution (indicated by the dashed line) is much higher than the observed one. The simulated intensity with the Gaussian convolution (indicated by the bold line)

reproduces the observed one. The simulated background intensity barely changes as a result of the Gaussian convolution, because the Si columns are separated by 0.27 nm from each other along the [100]-direction. Figure 4(b) shows the FWHM (defined by  $2.35\sigma$  in equation (1)) of the Si column at different thicknesses. The FWHMs were  $\sim 75$  pm at 10 nm thickness and increased linearly to  $\sim 95$  pm at 50 nm thickness. The FWHMs of the simulated images after the convolution (solid line) are similar to the observed ones.

## Discussion

### Z-contrast imaging in ADF with an incident beam of a large convergent angle

The detector inner angle used in the present experiment, 42 mrad, was relatively small for Z-contrast imaging in HAADF. In such case, ADF intensity can be affected considerably by elastic scattering and failed to give Z-contrast images [30]. However, we found a higher TDS intensity,  $I_{\text{TDS}}$ , than the coherent one,  $I_{\text{elastic}}$ , for the 42 mrad inner detector by

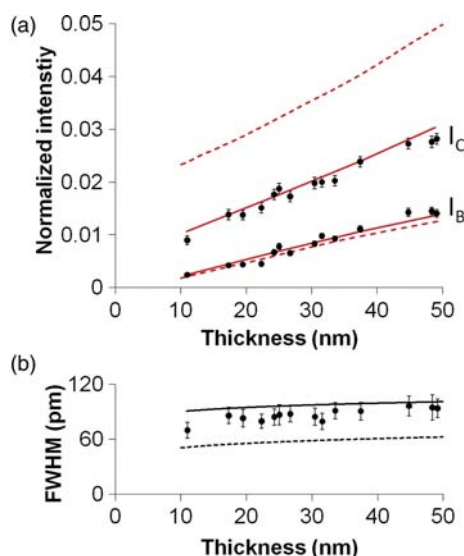


**Fig. 4.** (a) ADF intensity as a function of thickness from 10 to 50 nm. The average column intensities,  $I_C$ , taken from 14 ADF images are plotted as dots. They are lower than the calculated values taken from the simulated ADF images, indicated by the dashed line. The observed background intensities,  $I_B$  (dots), are similar to the calculated values (dashed line). By convoluting the Gaussian function of 70 pm (FWHM) with the simulation, the calculated column intensities decrease (solid line) and come in line with the observed intensities. (b) Average FWHM for the columns taken from 14 different ADF images as a function of thickness when column intensity is expressed as a two-dimensional Gaussian function. The experimental FWHMs are indicated by dots, which gradually increase with thickness. The simulated FWHM (dashed line) shows the same tendency as the experimental one but has smaller values. By convoluting the Gaussian function, the simulated FWHM (solid line) becomes similar to the experimental one. Error bars of each plot denote standard deviation of measurement uncertainty.

calculating the relative contribution of TDS to elastic scattering as will be shown below.

Figure 5(a) shows the intensity evolution of TDS (left panel) and coherent scattering (right

panel) with increasing specimen thickness. The intensity evolution of coherent scattering oscillated two times in the vicinity of the focal position (2 nm under the surface) and becomes lower for thicknesses greater than  $\sim 4$  nm. In addition, both intensity evolutions of TDS and coherent scattering rapidly increase up to  $\sim 4$  nm in thickness. The electron channeling effect must have occurred only in thicknesses up to  $\sim 4$  nm (see also Fig. 5(b)). This value (4 nm) is reasonable considering the improved depth resolution of the large convergent electron probe (depth of the field  $\sim 2$  nm [15]). Comparing their intensities, we found that ratio of TDS intensity to the elastic one,  $I_{\text{TDS}}/I_{\text{elastic}}$ , is about 40 for the thickness range 10–50 nm. The sum of TDS and coherent scattering is shown by the dotted line in Fig. 5(b), and this line corresponds to the simulated column intensity as shown by the dashed line in Fig. 4(a). Since it is almost the same with the intensity of TDS, the ADF intensity for this experimental condition is determined dominantly by TDS.

For the simulated intensity ratio,  $I_{\text{TDS}}/I_{\text{elastic}}$ , for detector inner angles of 35 mrad, the ADF intensity was determined by TDS against the coherent scattering and the ratio was  $\sim 10$  for thicknesses of 10–50 nm (not shown). However, a small-thickness oscillation in the total intensity appeared due to coherent scattering. As a result, we confirmed that the 42 mrad detector inner angle showed a Z-contrast image even with the 30 mrad convergent probe.

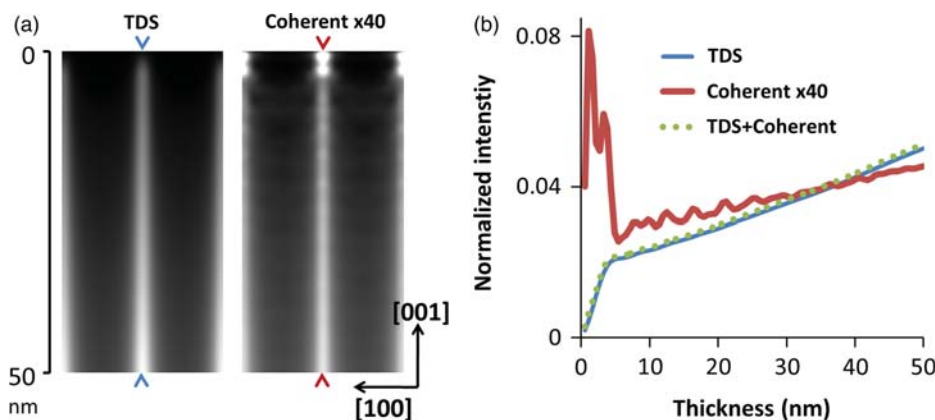


**Fig. 5.** (a) Intensity evolution of TDS and coherent scattering as a function of thickness. (b) Intensity evolution of TDS (solid line), coherent scattering (bold line) and the sum of TDS and coherent scattering (dotted line) as a function of thickness. The intensity of coherent scattering is shown at 40 times scale.

### Gaussian convolution

In the present study, we found that experimental images were reproduced by the simulation with 70 pm FWHM Gaussian convolution. In the previous quantitative studies, the FWHM of the Gaussian function convolved with the simulated image was estimated to be 80 pm for the SrTiO<sub>3</sub> crystal [19] and ~120 pm for the SrTiO<sub>3</sub> and PbWO<sub>4</sub> crystals [21], when the observation was done with a convergent beam of 10 mrad and detector having inner angles of 65 mrad. They suggested that the Gaussian convolution was required because of spatial incoherence such as the effective source size, mechanical instability of the microscope, drift, and so on [20,21]. Moreover, the two experiments on the SrTiO<sub>3</sub> [19,21] crystal had different FWHMs of 80 and ~120 pm. This difference was explained to be due to the Schottky field emitter degradation, which in turn influences the effective source size of the emitter [20]. We considered several effects that might cause the difference between the experiment and simulation in Fig. 4.

#### Effect of lattice vibration

It has been reported that the electron beam could heat a specimen during TEM/STEM experiment [31]. Therefore, lattice vibration could be increased during irradiation of highly dense electron beam in the STEM experiment and TDS intensity could be increased. Taking such an irradiation effect into account, we simulated the ADF intensity for a DWF of 1.0 Å<sup>2</sup>, which was higher than 0.46 Å<sup>2</sup> in the literature [29]. For DWF = 1.0 Å<sup>2</sup>, the column intensity decreased by 10% and the background intensity increased by 10%. The simulated image could not be matched the observation, because the background intensity after Gaussian convolution became too high. Therefore, we conclude that a DWF of 0.46 Å<sup>2</sup> is reasonable for the experimental result.

#### Effect of strain in the specimen

The effect of lattice strain on the ADF intensity was tested by simulation. The Si (001) specimen was strained with a maximum displacement of  $A = 0.1$  Å or 0.2 Å along the [100]-direction.

$$X_n = A \cos\left(\frac{2\pi na}{L}\right) \quad (2)$$

where  $X_n$ ,  $n = 0, 1, 2, \dots$ , is the displacement along the [100]-direction of the  $n$ th atom in the column,  $L$  is the specimen thickness, and  $a$  is the unit cell distance of 5.43 Å. These maximum displacements correspond to 3.5 and 7% strains, respectively, since the distance between two neighboring atoms is 2.7 Å along the  $\hat{a}_{100}$ -direction. As a result, the column intensity decreased at ~3 and ~10% for 0.1 and 0.2 Å, respectively.

#### Effect of sample preparation

Ion-milled samples were reported to be covered with amorphous damaged layers, and they gave blurred image intensities [26]. The column intensities in the ADF image of the ion-milled specimen fluctuated more than those in the images of the mechanically polished sample. For our ion-milled specimens, we needed a Gaussian function of about 100 pm in FWHM to match the observation with the simulation. Although the present mechanically polished specimen had less amorphous damaged layer than the ion-milled ones, Gaussian convolution size might partly be due to an amorphous layer on the specimen which was not completely eliminated during sample preparation process of mechanical polishing.

#### Effect of the source size

We estimated the effective source size, assuming the brightness of our CFEG source to be the reported value of  $1 \times 10^9$  A/(cm<sup>2</sup> s rad) [24]. In the present study, Gaussian probe size,  $S_{\text{Gauss}}$ , was 31 pm at an electron probe current of  $I_{\text{Probe}} = 30$  pA and convergent beam angle of  $\alpha = 30$  mrad by

$$S_{\text{Gauss}}^2 = 4 \ln 2 \frac{I_{\text{Probe}}}{B\pi^2\alpha^2} \quad (3)$$

The estimated Gaussian probe size (effective source size on the sample) of 31 pm is smaller than Gaussian convolution size of 70 pm.

In this study, we showed that the simulation with Gaussian convolution agrees well with the experiment performed at a constant probe current using spherical aberration-corrected microscope. Although our current data do not allow us to explain the Gaussian convolution size of 70 pm, further experiments at various probe currents could

tell us about the remaining factor accounted for the Gaussian convolution size.

## Concluding remarks

In summary, we measured the ADF intensity for silicon [001] crystals as a function of sample thickness from 10 to 50 nm by using a large angle convergent beam (30 mrad) with a probe current of 30 pA. We found that the multi-slice simulation are in accordance with the observed ADF images after convolving it with a Gaussian function of 70 pm in an FWHM. We also concluded that the effective source size is one of the factors that contribute to discrepancy in the ADF image intensity between the experiment and simulation.

## Acknowledgements

The authors also thank the Global COE Program for the financial support.

## Funding

This work is supported by the Japan Science and Technology Agency (JST) under the CREST project.

## References

- Voyles P M (2006) Imaging single atoms with z-contrast scanning transmission electron microscopy in two and three dimensions. *Microchim. Acta* **155**: 5–10.
- Benthema K V, Lupini A R, Kim M, Baik H S, Doh S, Lee J-H, Oxley M P, Findlay S D, Allen L J, Luck J T, and Pennycook S J (2005) Three-dimensional imaging of individual hafnium atoms inside a semiconductor device. *Appl. Phys. Lett.* **87**: 034104.
- Thompson K, Booske J H, Larson D J, and Kelly T F (2005) Three-dimensional atom mapping of dopants in Si nanostructure. *Appl. Phys. Lett.* **87**: 052108.
- Tanaka T, Sano K, Ando M, Sumiya A, Sawada H, Hosokawa F, Okunishi E, Kondo Y, and Takayanagi K (2010) Oxygen-rich  $\text{Ti}_{1-x}\text{O}_2$  pillar growth at a gold nanoparticle- $\text{TiO}_2$  contact by  $\text{O}_2$  exposure. *Surface Sci.* **604**: L75–L78.
- Oshima Y, Sawada H, Hosokawa F, Okunishi E, Kaneyama T, Kondo Y, Niitaka S, Takagi H, Tanishiro Y, and Takayanagi K (2010) Direct imaging of lithium atoms in  $\text{LiV}_2\text{O}_4$  by spherical aberration-corrected electron microscopy. *J. Electron microsc.* **59**: 457–461.
- Roy S and Asenov A (2005) Where do the dopants go? *Science* **309**: 388–390.
- Castell M R, Muller D A, and Voyles P M (2003) Dopant mapping for the nanotechnology age. *Nat. Mater.* **2**: 129–131.
- Voyles P M, Chadi D J, Citrin P H, Muller D A, Grazul J L, Northrup P A, and Gossmann H-J L (2003) Evidence for a new class of defects in highly *n*-doped Si: donor-pair-vacancy-interstitial complexes. *Phys. Rev. Lett.* **91**: 125505.
- Mueller D C and Fichtner W (2004) Highly *n*-doped silicon: deactivation defects of donors. *Phys. Rev. B* **70**: 245207.
- Komarov F F, Velichko O I, Dobrushkin V A, and Mironov A M (2006) Mechanisms of arsenic clustering in silicon. *Phys. Rev. B* **74**: 035205.
- Voyles P M, Muller D A, Grazul J L, Citrin P H, and Gossmann H-J L (2002) Atomic-scale imaging of individual dopant atoms and clusters in highly *n*-type bulk Si. *Nature (London)* **416**: 826–829.
- Pennycook S J, Lupini A R, Kadavanich A, McBride J R, Rosenthal S J, Puetter R C, Yahil A, Krivanek O L, Dellby N, Nellist P D L, Duscher G, Wang L G, and Pantelides S T (2003) Aberration-corrected scanning transmission electron microscopy: the potential for nano- and interface science. *Z. Metallkd.* **94** (4): 350–357.
- Benthema K V, Lupini A R, Kim M, Baik H S, Doh S, Lee J-H, Oxley M P, Findlay S D, Allen L J, Luck J T, and Pennycook S J (2005) Three-dimensional imaging of individual hafnium atoms inside a semiconductor device. *Appl. Rev. Lett.* **87**: 034104.
- Oshima Y, Hashimoto Y, Tanishiro Y, and Takayanagi K (2010) Detection of arsenic dopant atoms in a silicon crystal using a spherical aberration corrected scanning transmission electron microscope. *Phys. Rev. B* **81**: 035317.
- Kim S, Oshima Y, Sawada H, Hashikawa N, Asayama K, Kaneyama T, Kondo Y, Tanishiro Y, and Takayanagi K (2010) A dopant cluster in a highly antimony doped silicon crystal. *Appl. Phys. Exp.* **3**: 081301.
- Klenov D O, Findlay S D, Alle L J, and Stemmer S (2007) Influence of orientation on the contrast of high-angle annular dark-field images of silicon. *Phys. Rev. B* **76**: 014111.
- Klenov D O and Stemmer S (2006) Contributions to the contrast in experimental high-angle annular dark-field images. *Ultramicroscopy* **106**: 889–901.
- LeBeau J M and Stemmer S (2008) Experimental quantification of annular dark-field images in scanning transmission electron microscopy. *Ultramicroscopy* **108**: 1653–1658.
- LeBeau J M, Findlay S D, Allen L J, and Stemmer S (2008) Quantitative atomic resolution scanning transmission electron microscopy. *Phys. Rev. Lett.* **100**: 206101.
- LeBeau J M, Findlay S D, Wang X, Jacobson A J, Allen L J, and Stemmer S (2009) High-angle scattering of fast electrons from crystals containing heavy elements: simulation and experiment. *Phys. Rev. B* **79**: 214110.
- LeBeau J M, D'Alfonso A J, Findlay S D, Stemmer S, and Allen L J (2009) Quantitative comparisons of contrast in experimental and simulated bright-field scanning transmission electron microscopy images. *Phys. Rev. B* **80**: 174106.
- Ishizuka K (2002) A practical approach for STEM image simulation based on the FFT multislice method. *Ultramicroscopy* **90**: 71–83.
- Sawada H, Hosokawa F, Kaneyama T, Ishizawa T, Terao M, Kawazoe M, Sannomiya T, Tomita T, Kondo Y, Tanaka T, Oshima Y, Tanishiro Y, Yamamoto N, and Takayanagi K (2007) Achieving 63pm resolution in scanning transmission electron microscope with spherical aberration corrector. *Jpn. J. Appl. Phys.* **46**: L568–L570.
- Sawada H, Tanishiro Y, Ohashi N, Tomita T, Hosokawa F, Kaneyama T, Kondo Y, and Takayanagi K (2009) STEM imaging of 47-pm-separated atomic columns by a spherical aberration-corrected electron microscope with a 300-kV cold field emission gun. *J. Electron Microsc.* **58**: 357–361.
- Sawada H, Sannomiya T, Hosokawa F, Nakamichi T, Kaneyama T, Tomita T, Kondo Y, Tanaka T, Oshima Y, Tanishiro Y, and Takayanagi K (2008) Measurement method of aberration from Ronchigram by autocorrelation function. *Ultramicroscopy* **108**: 1467–1475.

- 
- 26 Okuno H, Rouvière J-L, Jouneau P-H, Bayle-Guillemaud P, and Daudin B (2010) Visualization of Tm dopant atoms diffused out of GaN quantum dots. *Appl. Phys. Lett.* **96**: 251908.
- 
- 27 Egerton R F and Cheng S C (1987) Measurement of local thickness by electron energy-loss spectroscopy. *Ultramicroscopy* **21**: 231–244.
- 
- 28 Marquardt D W (1963) An algorithm for least-squares estimation of nonlinear inequalities. *SIAM J. Appl. Math.* **11**: 431.
- 
- 29 Peng L-M, Ren G, Dudarev S L, and Whelan M J (1996) Debye–Waller factors and absorptive scattering factors of elemental crystals. *Acta Crystallogr. A* **52**: 456–470.
- 
- 30 Pennycook S J and Jesson D E (1991) High-resolution Z-contrast imaging of crystals. *Ultramicroscopy* **37**: 14–38.
- 
- 31 Libera M (1996) Local amorphous thin-film crystallization induced by focused electron-beam irradiation. *Appl. Phys. Lett.* **68**: 331–333.
-